Final Report

200 East Vadose Test Site
Hanford Washington

Electrical Resistance Tomography

Submitted
September 15, 2000
By

William Daily and Abelardo Ramirez
Lawrence Livermore National Laboratory
Livermore, CA 94550

Work performed under the auspices of the U.S. Department of Energy by the Lawrence Livermore National Laboratory under Contract W-7405-Eng-48.

Contents

1.0 Introduction 4
2.0 Site Layout 5
3.0 What is Electrical Resistance Tomography? 8
3.1 Finite Difference Mesh Used 8
4.0 Objectives for ERT work 9
5.0 ERT Results and Discussion 10
5.1 Error Analysis 10
5.2 Three-Dimensional Image of Site Before Experiment – Baseline Site Characterization 10
5.3 Time Dependant 2-D Imaging During Release 12
5.4 Three-Dimensional Images of Conductive Anomalies Associated with the Tracer Plumes 13
5.5 Comparison of ERT Tomographs with Neutron Data 17
5.6 Changes in Moisture Content and In Pore Water Ionic Strength Based on Electrical Resistivity Changes 20
5.7 Possible Tank Farm Deployment Scenarios—Using Existing Steel Casings as Electrodes 25
6.0 Summary and Conclusions 31
7.0 Recommendations 32
8.0 References 33

Figures

Figure 2.1. Layout of the Site in Plan View 6
Figure 2.2. Layout of the Site in Perspective Showing the ERT Arrays and an Example of the Image Volume 7
Figure 5.1. Effects of Data Errors on the ERT Reconstruction Results 11
Figure 5.2. Reconstruction Attempt of the Baseline ERT Data 12
Figure 5.3. Effects of the Multiple Steel Casings on ERT 14
Figure 5.4. Schematic Representation of the Effects of Steel Casings at the site 15
Figure 5.5. Four Views of a Comparison Image of Changes in Electrical Resistivity Distribution as a Result of Spills 1 and 2 16
Figure 5.6. Four Views of the ERT Image Shown in Figure 7 with the Addition of Resistivity Increases Greater than 10% over Baseline 17

Figure 5.7. Four Views of a Comparison Image of Changes in Electrical Resistivity Distribution as a Result of Spill 3 18

Figure 5.8. Comparison of the ERT and Neutron Data Showing the Plume from Spills 1 and 2 19

Figure 5.9. Comparison of the ERT and Neutron Data Showing the Plume from Spill 3 20

Figure 5.10. Comparison of the ERT and Neutron Data Showing the Plume from Spills 1 and 2 23

Figure 5.11. ERT Images of the Effects of Mixing of Tracer Water and Native Pore Water 25

Figure 5.12. Four Views of the Electrical Anomaly from Spill 1 Reconstructed Using only the Steel Casings as Electrodes 27

Figure 5.13. Four Views of the Electrical Anomaly from Spills 1 and 2 Reconstructed Using only the Steel Casings as Electrodes 28

Figure 5.14. Four Views of the Electrical Anomaly from Spill 3 Reconstructed Using only the Steel Casings as Electrodes 29

Figure 5.15. ERT of Spill 3 Using Data as they Might be Available at a Tank Farm 30

1.0 Introduction

This report covers the electrical resistance tomography (ERT) work performed at the Hanford Reservation, 200 East Area Vadose test (Sisson and Lu) site, during the period May 1 through September 1, 2000.

The purposes of the ERT work were to

- image the electrical resistance distribution of the site before the test and use this information to infer site characteristics
- use the resistance images to infer the dynamics of the plume during at least one release
- determine the influence of the steel casings at the site on the ability to construct usable ERT images
- infer the distribution of the moisture content changes from at least one release
- determine if the steel casings at the site can be used as electrodes to provide useful images of at least one release.

2.0 Site Layout

A plan view of the well locations at the test site is shown in Figure 2.1. Eight ERT wells are arranged around the periphery with a single ERT well 2 m from the center of the pattern. Applied Research Associates using a cone penetrometer method installed these wells. Each well consists of 15 stainless steel electrodes spaced 1 meter apart (from center to center) between the depths of 19 and 5 m (see Figure 2.2). The purpose of these electrodes was to produce two dimensional (2-D) and 3-D images of the test site using ERT. Using data from array pairs (e.g., C and J) we surveyed vertical 2-D image planes. Using data from electrodes at a single depth (e.g., electrode at 7-m depth from each array: A through H and J), we also surveyed horizontal 2-D image planes. Combining all this data together, we hoped to get fully 3-D reconstructions of an image block bounded between 5- and 15-m depths and defined in plan view in Figure 2.1.

In addition to these "point electrodes," 24 steel casings (A1,A3, A5, B2, B4, B6, C1, C3, C5, D2, D4, D6, E1, E3, E5, F2, F4, F6, G1, G3, G5, H2, H4, H6) installed for a previous test at the site were used as "long electrodes." The purpose of these electrodes was to determine the feasibility of using steel casings present in tank farms for ERT imaging. Using data from these electrodes, we hoped to get 2 D images of horizontal plume structure only (no sensitivity to vertical structure).

Notice that the four ground-penetrating radar (GPR) holes are arranged in the southeast quadrant of the pattern. The tensiometer network is also concentrated in the same quadrant. Thermal neutron data (calibrated to yield moisture content) were acquired in each of the steel casings, and so these data yield site-wide and fairly uniform coverage. Because of its site-wide coverage, we have found the neutron moisture measurements valuable for some combined calculations with the 3-D ERT images.

Data-acquisition trips to the site were planned to yield the maximum information from the overall test with the minimum travel costs. Site visits occurred on May 26th (baseline), during the1st release on June 1st, during the 3rd release on June 15th, and after the spill sequence ended on July 11th. With this strategy, we collected before, during, and after data for Releases 1 and 3, and before and after data sets for combined releases 1-2, 1-2-3, and 1-2-3-4-5.

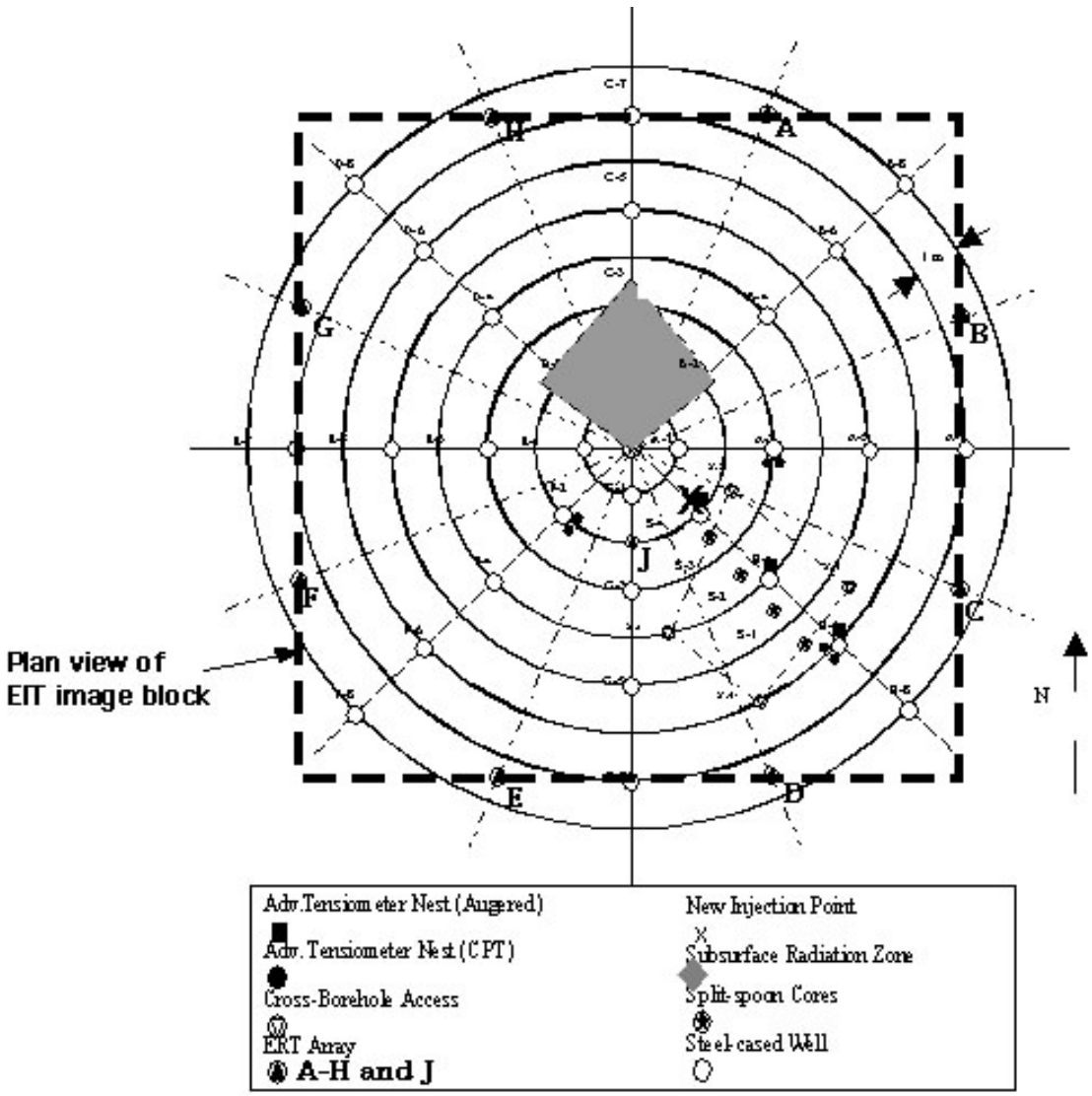

Figure 2.1. Layout of the Site in Plan View

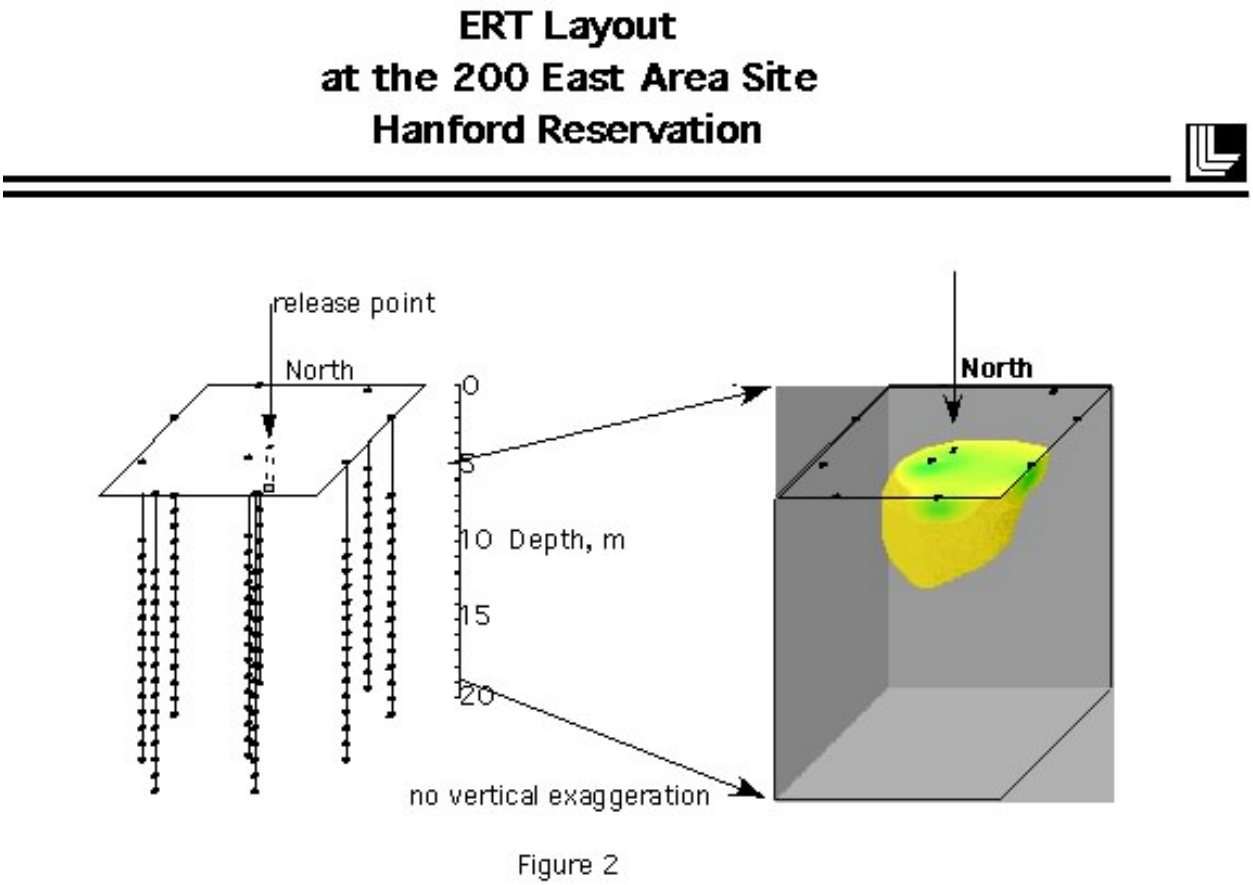

Figure 2.2. Layout of the Site in Perspective Showing the ERT Arrays and an Example of the Image Volume

3.0 What is Electrical Resistance Tomography?

ERT is a technique for imaging the subsurface electrical structure using conduction currents. From a series of electrodes, low frequency electrical current is injected into the subsurface, and the resulting potential distribution is measured. A large variety of different source and receiver orientations are used to sample the target volume from many different views. From that data, a computer model of the electrical-resistivity distribution is found that produces, to within some predetermined tolerance, the measured potential field. ERT was proposed 22 years ago independently by Henderson and Webster (1978) as a medical imaging modality and by Lytle and Dines (1978) as a geophysical imaging tool.

Early development in geophysics was confined to imaging rock core samples in the laboratory (Daily et al. 1987), but prototype data-collection hardware and research-grade inverse codes suitable for field-scale applications soon followed (Ramirez et al. 1993). More recently, ERT has been developed to detect leaks from large storage tanks (Ramirez et al. 1996), monitor underground air sparging (LaBrecque et al. 1996a) and map movement of contaminant plumes (Daily et al. 1998). During this entire period, data-acquisition hardware and inversion algorithms have been rapidly improving to handle the new challenges.

The ERT algorithm we used is based on an Occam's type inversion that yields a minimum roughness solution consistent with the data and their errors. The 2-D algorithm, based on a finite element forward solver, is described by LaBrecque et al. (1996b). Also discussed are mesh requirements used for both the 2-D and 3-D algorithms. A simple generalization of this approach to three dimensions is not practical, being computationally inefficient. However, LaBrecque et al. (1999) describe a method for streamlining the forward solver using an iterative finite difference formulation and a method to reduce the computational load associated with the Occam's approach. These changes make 3-D inversion practical. Convergence for both algorithms is achieved when the root mean square error, normalized by the weights, is equal to the number of data.

3.1 Finite Difference Mesh Used

The finite difference mesh used consisted of 40 elements in X, 40 elements in Y, and 43 elements in Z. Within the region of interest (the region completely surrounded by boreholes), there were 20 elements in X, 20 elements in Y, and 34 elements in Z. A total of 135 electrodes was included in the problem. In addition, the 33 steel casings present at the test site were modeled as regions of low electrical resistivity having a contrast of 10^{-4}:1 relative to the surrounding soil. In reality, the contrast between the steel casing and the soil is in all likelihood much larger; we chose to model the casings with a more modest contrast in order to prevent numerical instabilities in the forward solver. The size of the voxels in the region of interest was 0.67 m in X, 0.67 m in Y, and 0.5 m in Z.

4.0 Objectives for ERT work

The objectives of the ERT work support the overall objectives of the vadose test:

1. Produce time-dependent 2-D imaging of a developing plume during the release of the tracer. Two-dimensional imaging was desired so that data-acquisition times were fast enough to capture the plume at various stages of development.
2. Evaluate the possibility of using the existing steel casings at the site as long electrodes. This approach would yield only 2-D images of the site but is of interest because of its potential use in a single shell tank farm where such casings exist and where installing more ERT electrodes is cost-prohibitive.
3. Produce 3-D images of plumes resulting from increased moisture content after a tracer release. From these data and a petrophysical model relating resistivity to moisture content, we would generate images of moisture-content change.
4. Produce 3-D images showing the electrical resistivity distribution of the test site before any tracer releases. This would show the resistance structure from which basic lithology (e.g., distribution of clays, fines, gravel) could be inferred.
5. Estimate the released mass of tracer using an ERT image.
6. Make a quantitative estimate of the noise in the data and its effect on reconstructed images.
7. Estimate the amount and distribution of mixing between the native pore water and the tracer water.
8. Look for unexpected results. Two such results were found: (a) regions form during the tracer infiltration in which the local resistivity actually increases while the neutron data suggest a decrease in moisture content and (b) the numerous steel cased wells at the site have a serious and heretofore unappreciated “shorting” effect.

5.0 ERT Results and Discussion

5.1 Error Analysis

A defensible interpretation of ERT requires an estimate of the measurement errors and determination of their effect on the reconstructed images. Although it is not possible to measure the data errors, we have found that reciprocity yields the best *estimate* of data error. (The reciprocal of a measurement is made by interchanging the source and receiver dipole locations.) If reciprocal pairs of measurements (we will call one "normal" and the other "reciprocal") are identical, we will assume that they are error free. Of course, the pair are never identical, and we assume the difference is a measure of the error. Because we need the effects of these errors on the images, our procedure is to use the normal data to calculate an image and then the reciprocal data taken at the same times to calculate an image. The differences in these tomographs produce an estimate of the effects of error on them, and this information can be used to yield a defendable interpretation.

Figure 5.1 shows the comparison image for Spill 3 where the reconstruction is accomplished using only the normal measurement of transfer resistance measured before and after the spill. Part b of that figure is the comparison image using only the corresponding reciprocal data. To show the differences in these tomographs, Figure 5.1c is the voxel by voxel ratio of these reconstructions, $\rho_{normal}/\rho_{reciprocal}$, with all voxels greater than 0.9 (10% differences between voxels) made transparent. We see that errors propagate through the analysis to create some differences in the two images of more than 10%. As Figure 5.1d shows, there are no voxels of value less than 0.8 (20% difference). Our experience suggests that a 20% error is unusually high; typically the errors are around 5%. The reason for this unusually high level of error is unclear. Perhaps it is caused by the presence of numerous metallic casings at the site. We propose a 20% level of reliability in our results and adopt this level as the noise discriminator for all of the tomographs presented here, claiming that $0<=f<=0.8$ are reliable decreases in the subsurface resistivity distribution and $0.8<f$ are caused by data errors.

5.2 Three-Dimensional Image of Site Before Experiment - Baseline Site Characterization

The most accurate analysis we can do with the ERT data is a full 3-D inversion. This required a large amount of highly accurate data (reciprocal to at least 1%). We combined data taken from several subsets of the 135 available electrodes (15 electrodes in nine different arrays). Fifteen subsets were taken using the nine electrodes at a common depth in 1-m increments between 5- and 19-m depths. Nine subsets were taken with 30 electrodes from the eight pairs of arrays forming vertical planes radiating from array J (see Figure 2.1). Taken together, these amounted to 7290 measurements for each 3-D image, and this took about 5.5 hr to acquire.

The first 3-D data set was taken May 26th as a baseline for the experiment. We have been unsuccessful in all our efforts to invert this data set and image the baseline resistivity structure. This is unfortunate because with success we should have a 3-D representation of the resistivity whereas now we have only a series of 1-D sections provided by Applied Research Associates.

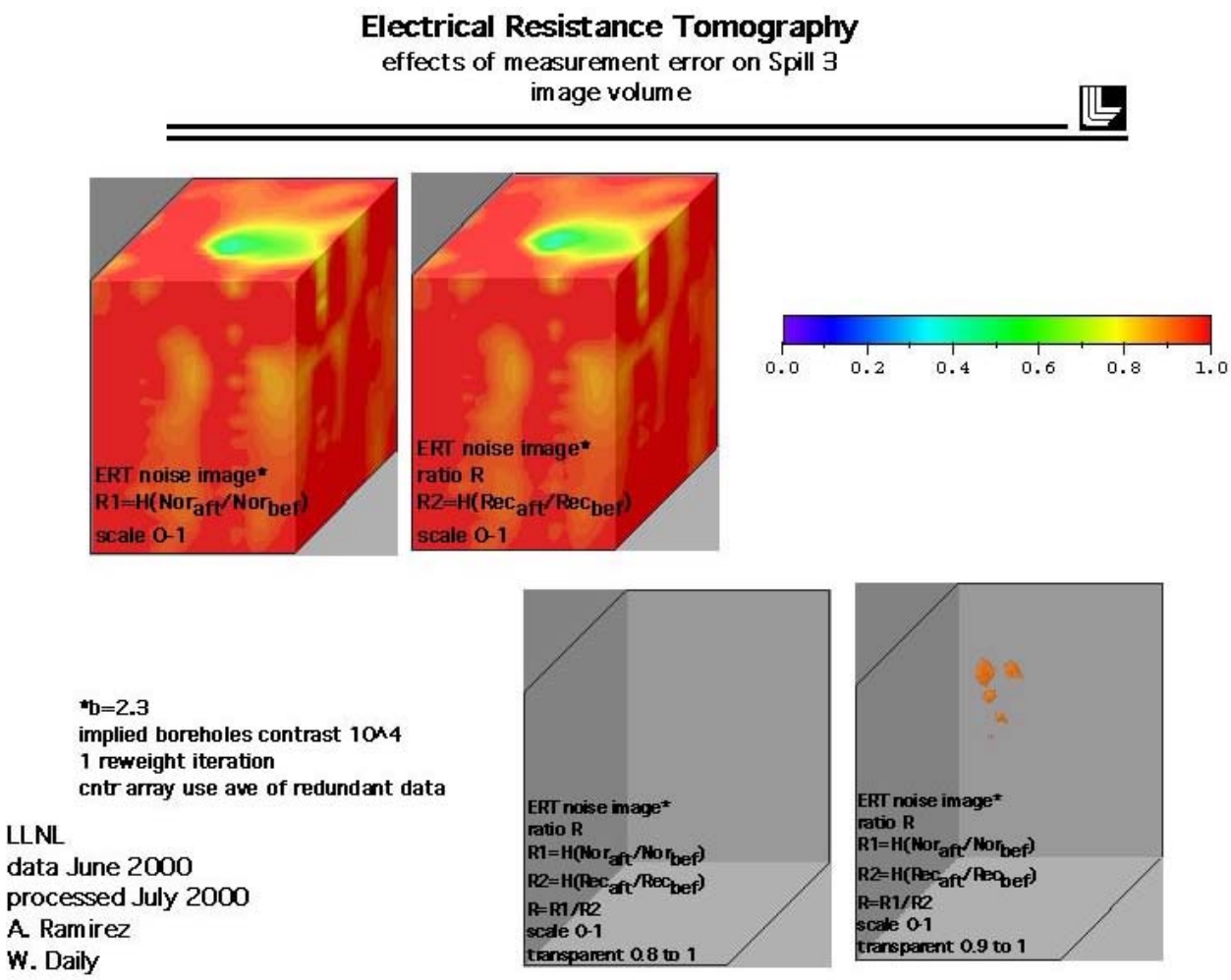

Figure 5.1. Effects of Data Errors on the ERT Reconstruction Results. The normal and reciprocal measurements, respectively, are used for the two comparison reconstructions at the top left. Error-free data and a perfect analysis would yield identical images. A voxel-by-voxel comparison of these images is shown at lower right-—at the 80% and 90% confidence level. At 80% confidence (corresponding voxels are within 20% of each other), the two reconstructions are the same (lower left).

We believe the reason for the failure to invert the baseline data is the presence of the numerous steel casings present at the site. These casings are 10^4 to 10^8 times more electrically conducting than the soil. Thus, they produce a very large contrast in electrical properties within the image volume. These casings are also complicated in their resistivity properties because they contain layers of fresh and rusted metal; the thickness and exact resistivity properties of these layers are unknown variables along a casing's length. To date, we have been unable to find a value to allow convergence. One attempt is shown in Figure 5.2.

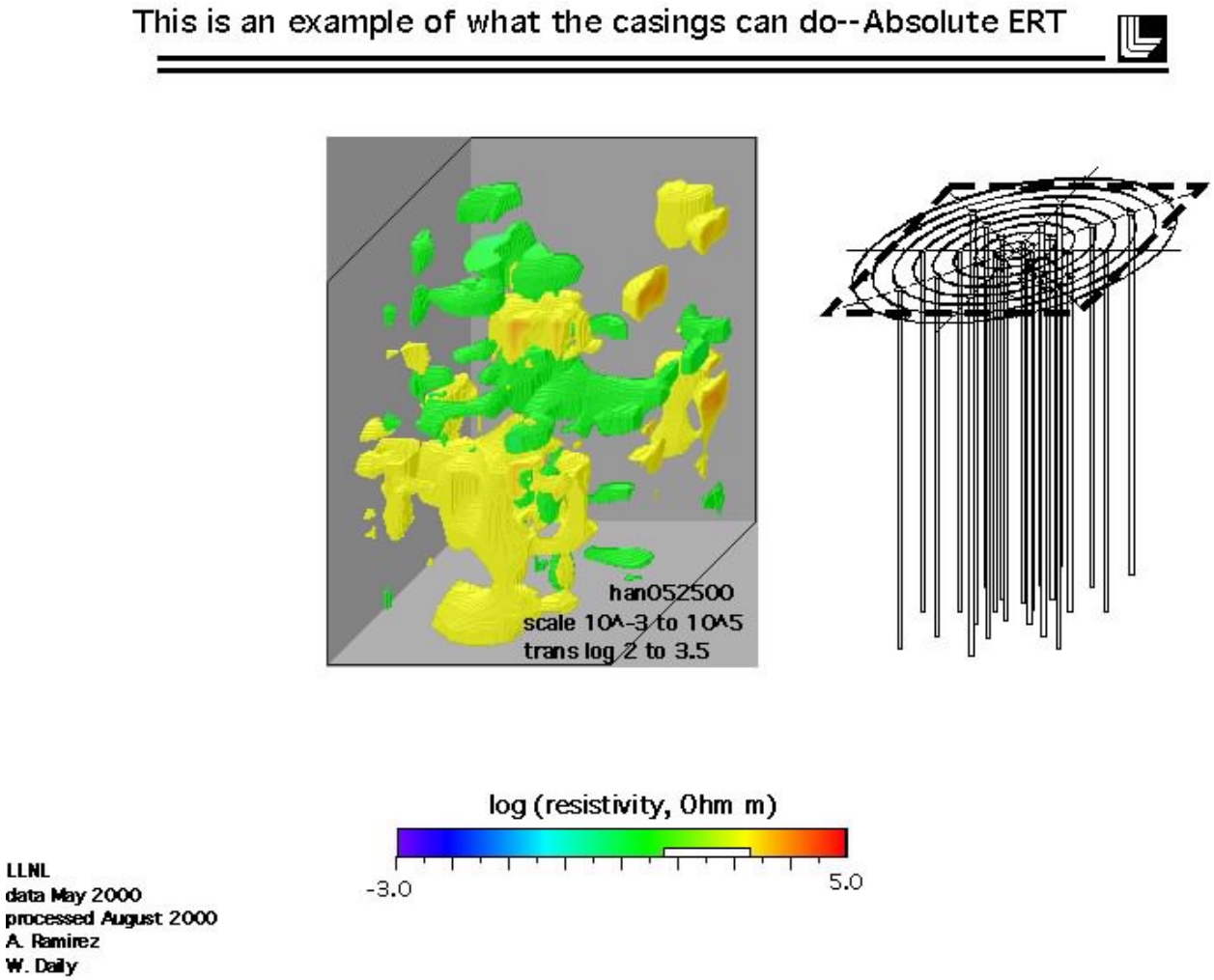

Figure 5.2. Reconstruction Attempt of the Baseline ERT Data. This reconstruction did not converge because of the effect of the multiple steel wells (on the right).

5.3 Time Dependant 2-D Imaging During Release

During releases 1, 3, and 5, we took data as a function of time to determine the details for the growth of the plume of enhanced moisture content. Data were taken in 15 horizontal planes using nine ERT electrodes at each common depth, with the objective of reconstructing a 2-D image for each plane. We successfully reconstructed values of transfer resistance R_D measured during the release, after modifying each value as follows:

$$R_D\,(R_H/R_B) \tag{1}$$

where (R_H/R_B) is a ratio of corresponding transfer resistance values from a homogeneously resistive half-space model and the baseline value. The reason for this procedure is the empirical discovery that it

removes from the reconstructed image some of the effects of boundary conditions that cannot be exactly modeled by the forward solver in the code (i.e., the high-conductivity effects of the steel cased boreholes). However, the results of such processing were not successful in rendering time-dependent behavior of the plume development.

The effects of the steel casings are shown in Figure 5.3. In the horizontal planes on the left, notice the conductive anomalies in the bottom plane about 15 m below the release point (19-m depth). Consider next a 3-D reconstruction shown in the center using data from all horizontal and the vertical planes. Notice the conductive anomaly directly below the release point but also the ring-shaped anomaly at the image block bottom. This 3-D reconstruction does not include effects of the vertical steel casings at the site in the model that produces R_H,. We believe these steel casings artificially cause the lower anomaly in the 3-D reconstruction as well as the anomalies in the lower 2-D reconstructions (at the left). This hypothesis is supported by the result in Figure 5.2 on the right. This is a 3-D reconstruction like the center image except that the finite difference model producing R_H is modified to contain vertical conductances that account for the electrical effects of the steel casings. Notice that for this case, the lower anomaly is absent, but the conductive anomaly from the tracer at shallower depths is unchanged.

When the effects of steel casings on the electrical current flow are not included in the data processing (Figure 5.3), a phantom anomaly(s) appears below the actual anomaly. The reason for this phenomenon is that the casings cause subsurface electrical short circuits. This is described schematically in Figure 5.4. A conductive plume changes the electrical connection at the top between two casings. Because of the casing's high conductance, measurements made near the bottom are sensitive to changes in resistivity at shallow depths. The net effects are a vertical "smearing" of features, the magnitude of the problem depending on details such as the contact resistance between the casing and the soil, but the effect is the artificial placement of conductive anomalies at depths that are phantoms of real anomalies. This effect was an unexpected discovery during data processing.

What is the solution to this shorting effect from the casings? Short of removing the steel casings from the site, we believe there is no perfect solution. A partial solution is to correctly model these casings in the data analysis. This approach allows the numerical model to account for the most of the casing effects, thereby minimizing the presence of phantoms in the image.

Our 2-D-inversion code cannot model the effects of the steel casings at the site because the casings make the current flow 3-D. Therefore, we are unable to use the data taken during any release to produce 2-D horizontal images of the time-dependent development of a plume.

5.4 Three-Dimensional Images of Conductive Anomalies Associated with the Tracer Plumes

Data that allow fully 3-D were acquired on May 26th (as a baseline), June 1st (right after the first release ended), June 14th (just before the 3rd release), June 16th (a day after the 3rd release), and July 11th (after the 5th release). As discussed above, we have not been able to invert any of these data sets in absolute sense because of the steel casings at the site. However, we have been able to use the approach described by equation (1) to invert for comparison images. Under these conditions, the algorithm is much less sensitive to partially inaccurate representations of the casings. The result of this ratio technique is an image of fractional comparison for each reconstructed voxel $f = \rho_t / \rho_{base}$. For example, if $f = 1$, the

resistivity ρ_t has not changed from the baseline value ρ_{base}. When $f = 0.8$, the resistivity has decreased to 80% of the baseline value.

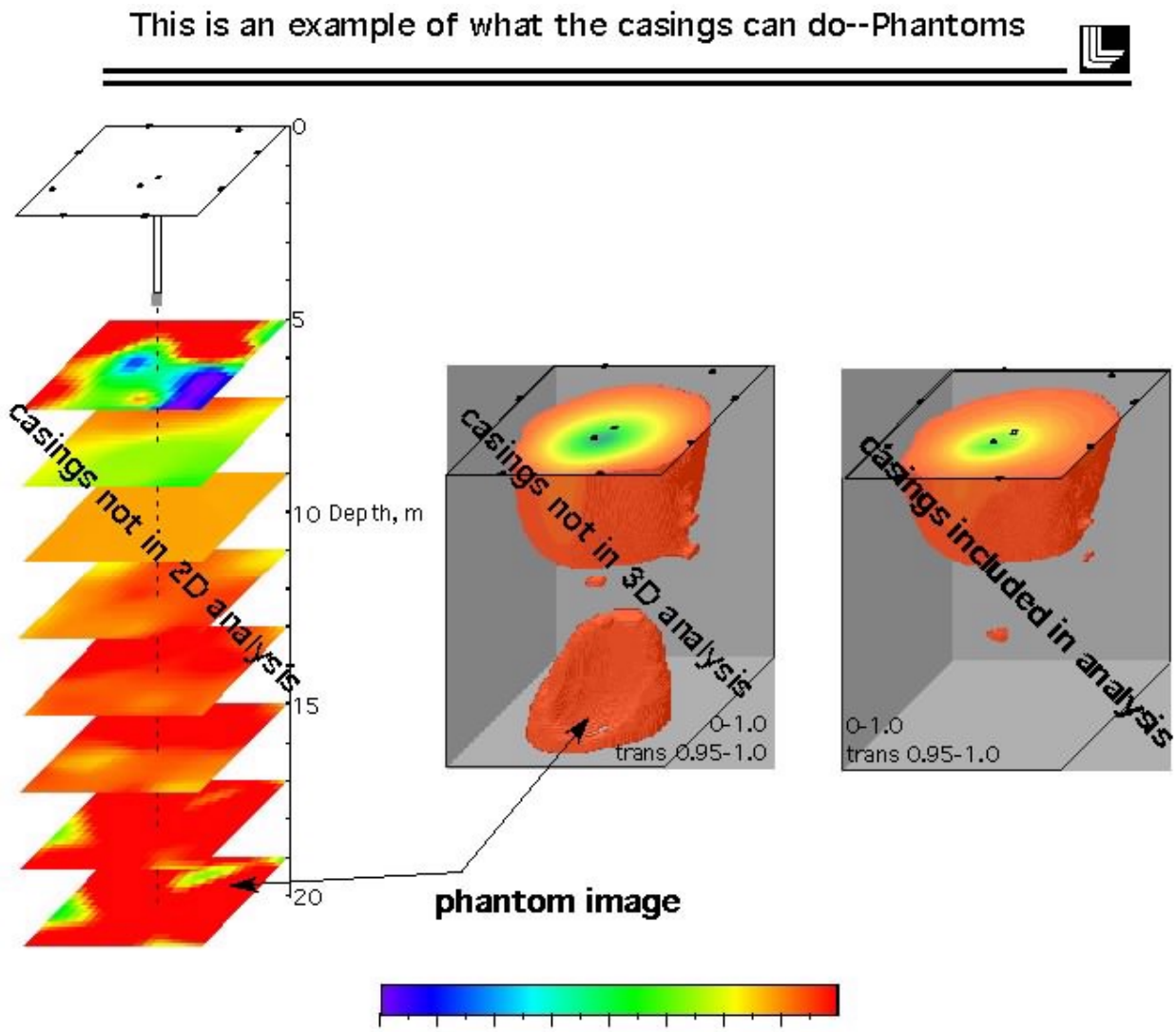

Figure 5.3. Effects of the Multiple Steel Casings on ERT. At the left are several horizontal 2-D image planes that are processes without the steel casings in the modeling. In the center is a 3-D comparison image reconstructed without the steel casings in the forward model. On the right is the same 3-D comparison image reconstructed including the steel casings in the forward model.

Figure 5.5 shows the conductive anomaly resulting from the ratio comparison of data from May 26th and June 14th and therefore has the combined effects of releases 1 and 2. (It was not possible to use the data from June 1st because they were taken the same day as the water release, and the subsurface resistivity was still changing significantly over the interval of 5.5 hr required to acquire the data. As a

result, the data are internally inconsistent, and the inverse algorithm cannot find to a solution.) These inversion data were combined from the 8 pairs of radial planes (using pairs of peripheral arrays and the center array) and 15 horizontal planes (using the nine electrodes at each common depth).

Steel casings at the site can produce phantoms

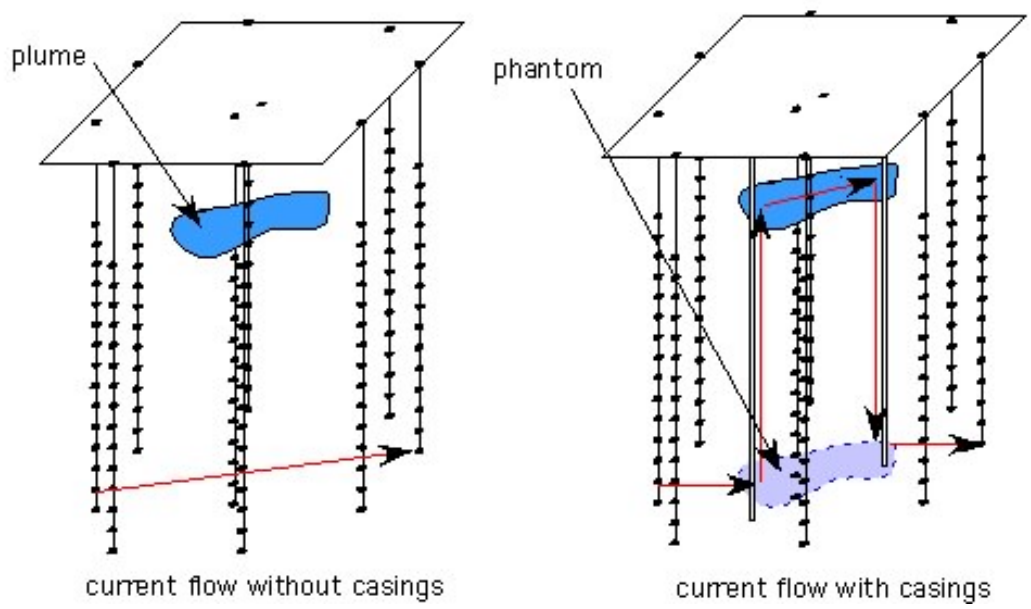

Figure 5.4. Schematic Representation of the Effects of Steel Casings at the site. On the left is a representation of how current might flow between electrodes without the interference of the steel casings. On the right is the same situation but with two casings that will shunt some current through the anomaly higher in the image block.

The image block has been edited so that all voxels $f <= 0.8$ are rendered transparent. These transparent voxels are those that represent changes in resistivity smaller than what is empirically reliable. In other words, the isocontour surface represents that surface at which the changes become reliable (above the error level). Four views are shown to help the 3-D visualization of the volume. The anomaly extends between about 6-m to 12-m depth, directly below the spill point. Although there is a smaller anomaly lower in the section, there is no good evidence for a fast path of flow below 12-m depth.

Below the release point, the conductive anomaly does not extend to the top of the image block as might be expected to result from a release just above the block. Instead, as Figure 5.6 shows, directly below the release is a small anomaly of increased resistivity ($f > 1.0$). If this region has higher moisture content, then the resistivity could increase if the ionic content of the pore water has been decreased. We

believe that the relatively clean tracer water (river water of conductivity 1.4×10^2 microSeimens/cm) diluted or flushed ions in the original pore water very close to the release point, increasing the saturation, but causing a net increase in resistivity (Figure 5.6). Further from the release point, the dilution effect was less or ions were flushed into these regions, and we see the anomaly of decrease in resistivity (Figure 5.5).

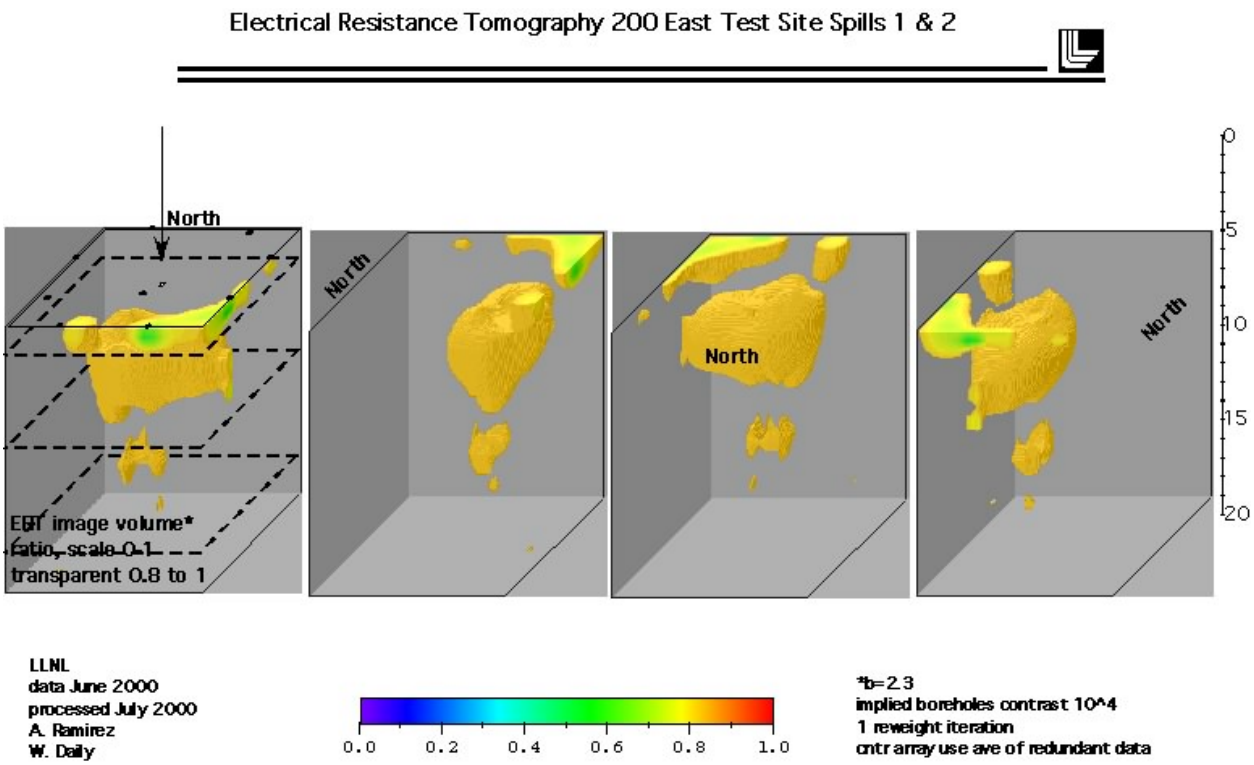

Figure 5.5. Four Views of a Comparison Image of Changes in Electrical Resistivity Distribution as a Result of Spills 1 and 2. The anomaly is shown as an isosurface at the 80% confidence level (see Figure 5.1). On the left view is superimposed the approximate location of three conductive layers as seen in the resistivity logs.

Figure 5.7 shows the conductive anomaly resulting from the ratio comparison of data from June 14th and 16th. Therefore, this image has the effects of the third release only (KBr added to the water released). Here also the image block has been edited so that all voxels $f <= 0.8$ are rendered transparent. In contrast to the fresh water releases, the conducting anomaly extends past the top of the image block—there is no evidence of a resistive anomaly directly below the release point because the tracer water was enriched in KBr ions to a conductivity of 2.1×10^3 microSeimens/ cm or approximately 15 times more conducting than the fresh water tracer. As for Release 1 and 2, the anomaly is directly below the spill point and extends between about 6-m to 12-m depth. Although there is a small appendage lower in the section, there is no good evidence for a fast path of flow through the block.

5.5 Comparison of ERT Tomographs with Neutron Data

It was desirable to compare the ERT results with the neutron data in a format that allowed easy comparisons. Researchers at Pacific Northwest National Laboratory have collected the neutron data. We used 3-D plots of interpolated neutron data in the same image block used for ERT display. This was accomplished using a well-known commercial software called Earth Vision (Version 5.1), which uses a minimum tension interpolation technique to render a 3-D volume. Minimum tension is the distribution of tension (the second derivative or curvature of the property variation) along the nodes such that the sum of the squares of the second derivatives is minimized. This approach honors the value of the input data as closely as possible and yields "natural" looking models of the property variation.

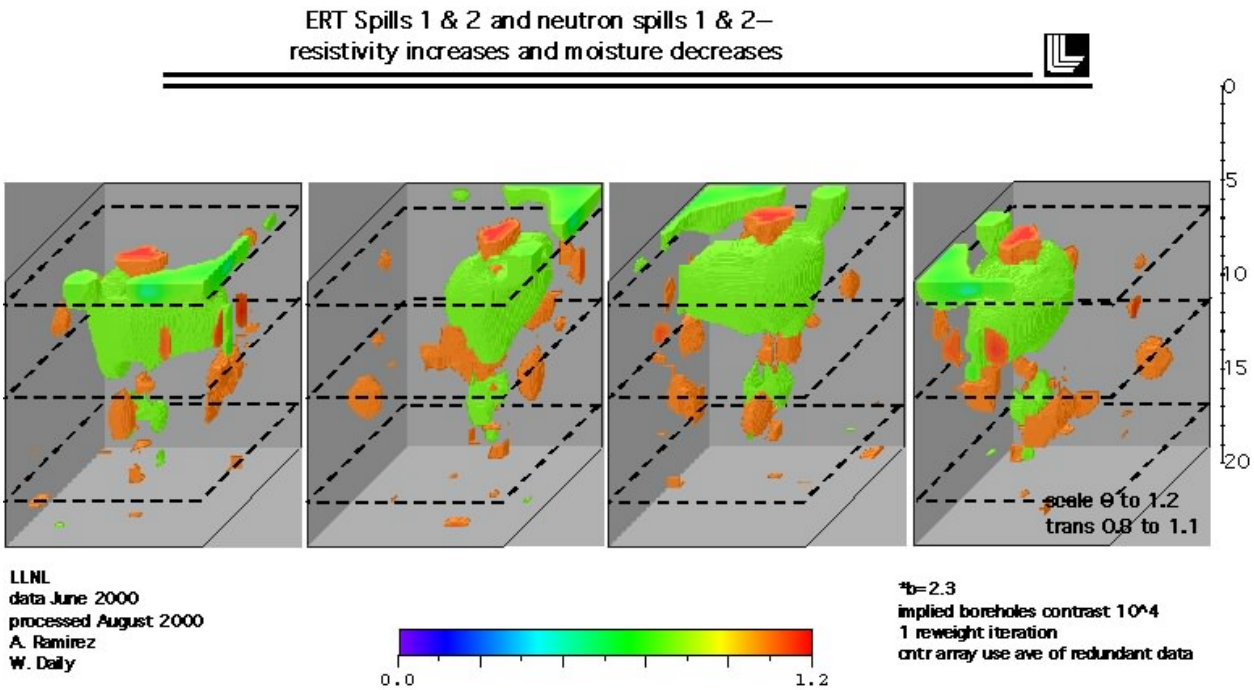

Figure 5.6. Four Views of the ERT Image Shown in Figure 7 with the Addition of Resistivity Increases Greater than 10% over Baseline

Figure 5.8 shows the differences in volume percent water content generated by subtracting the neutron data taken on the 5th of May (baseline) and the 9th of June (after the second spill). For convenience, the corresponding ERT anomaly (from Figure 5.5) is shown here also. Except for the portion at the top of the image block, there is general correspondence between the two data sets. A more careful comparison is done along the side of Figure 5.7 where neutron contours overlay horizontal slices of the ERT image at 2-m increments between 5- and 19-m depths. At 5-m depth, the ERT images show water moving out the south and East Side of the block, although the neutron image does not support that. We have no explanation for the discrepancy. As discussed above, the absence of a conducting anomaly that would correspond to the neutron anomaly may be due to the removal of ions from pore water just below the release point. At 7-m depth, the conductive anomaly is starting to appear with the neutron

anomaly. The correspondence between the two is good at 9-m depth. Below 11-m depth, neither ERT nor neutron data show significant tracer water.

The same ERT-neutron comparison for Spill 3 is shown in Figure 5.9. At this point in the experiment, there is still good correspondence, but the explanation becomes more complex. In this case, the neutron data are sensitive to the changes in saturation, whereas the resistivity data are sensitive to changes in saturation and changes in pore-water salinity. The ERT anomaly (from Figure 5.7) is strong and compact as a result of the higher conductivity of the tracer water. However, the moisture anomaly is fragmented where the earlier moisture anomaly was located but has now grown downward. The original moisture plume (from Spills 1 and 2) left the sands at a high saturation. The additional water of Spill 3 could only minimally increase the saturation level so the neutron data sees no increase (see Figure 5.9, especially the horizontal slices along the right hand side of the figure). The extra water of Spill 3 causes the plume to grow mostly downward, and the lower portion is what shows up in this difference view.

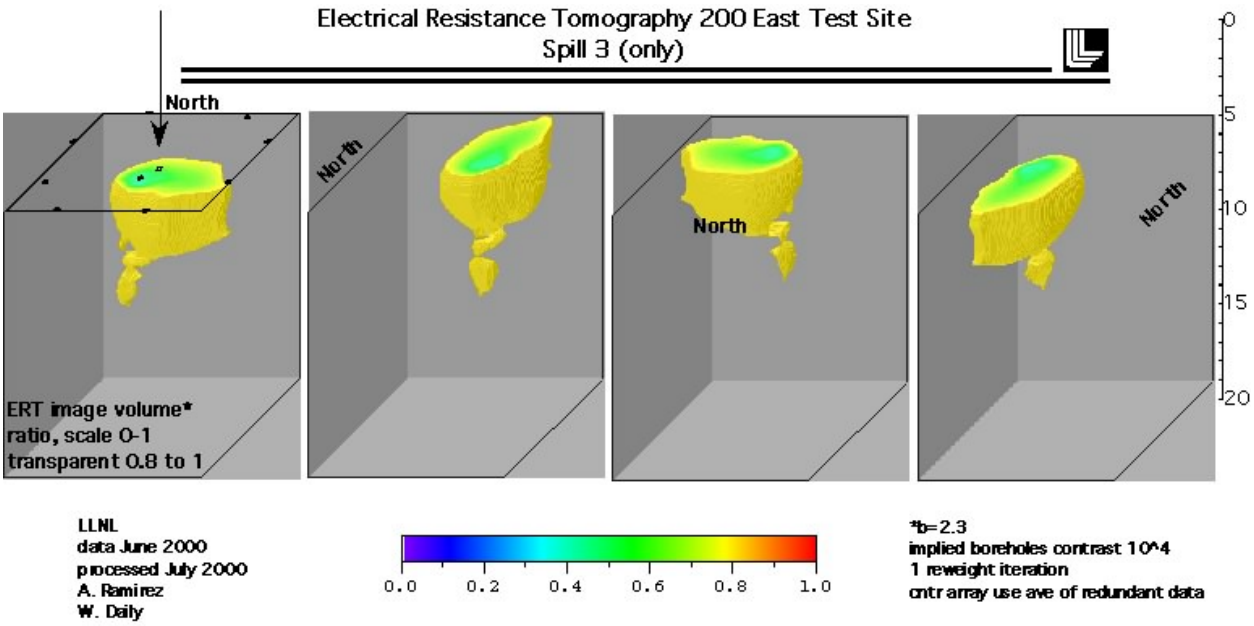

Figure 5.7. Four Views of a Comparison Image of Changes in Electrical Resistivity Distribution as a Result of Spill 3. The anomaly is shown as an isosurface at the 80% confidence level.

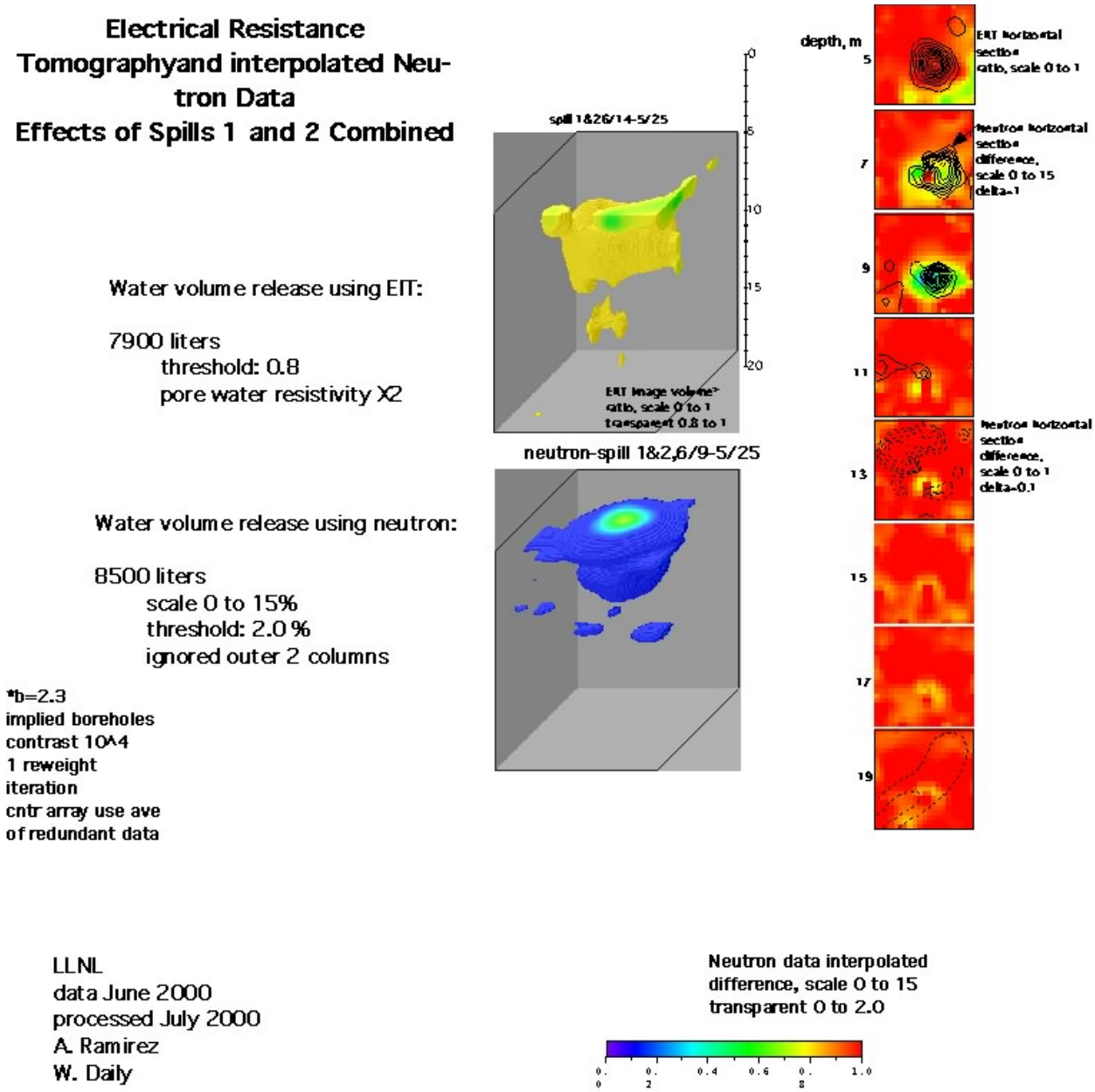

Figure 5.8. Comparison of the ERT and Neutron Data Showing the Plume from Spills 1 and 2. The top left is the ERT image of the electrical anomaly. Below that is the corresponding plume generated from an interpolation of the neutron data. On the right are horizontal slices from the ERT image overlayed with contours of moisture content inferred from the neutron data.

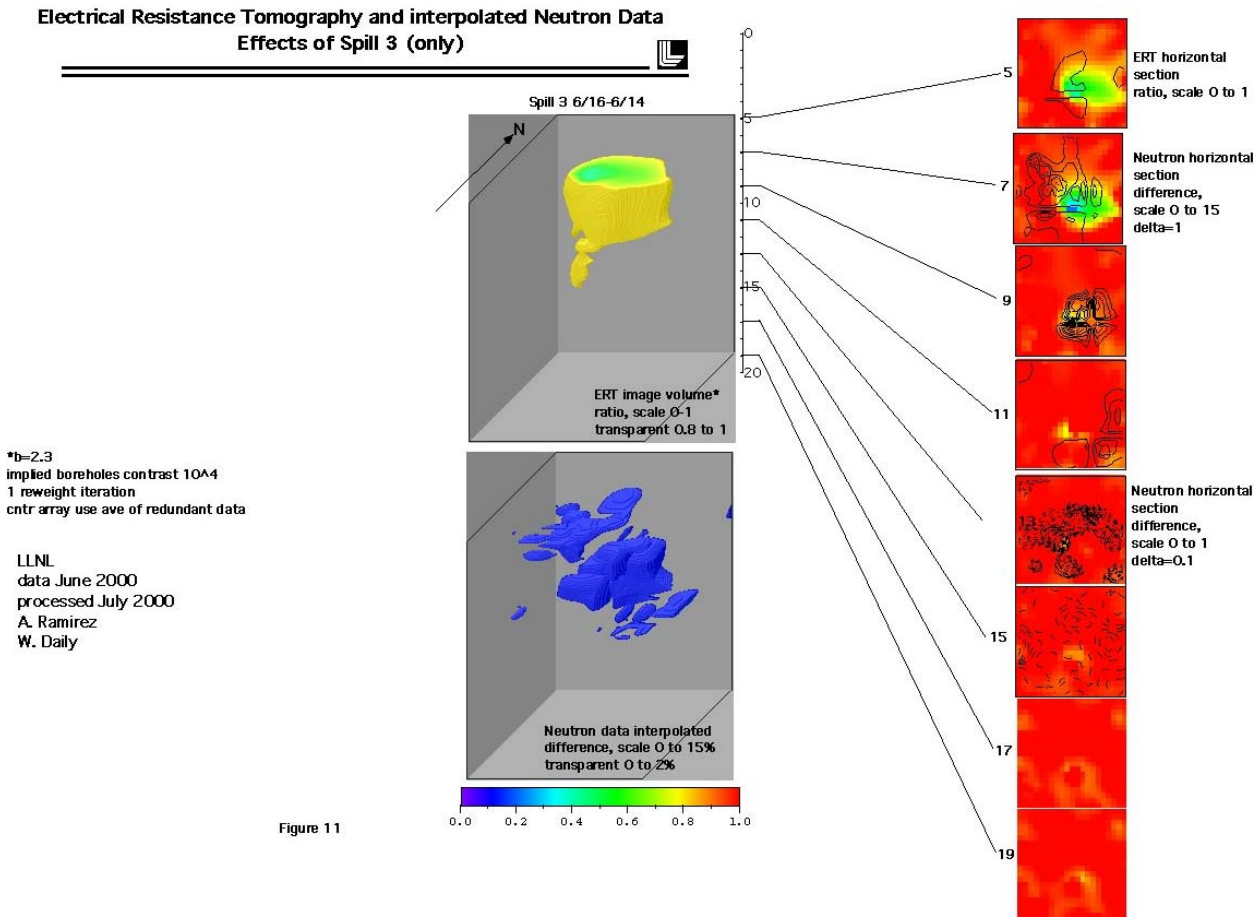

Figure 5.9. Comparison of the ERT and Neutron Data Showing the Plume from Spill 3. The top left is the ERT image of the electrical anomaly. Below that is the corresponding plume generated from an interpolation of the neutron data. On the right are horizontal slices from the ERT image overlayed with contours of moisture content inferred from the neutron data.

5.6 Changes in Moisture Content and In Pore Water Ionic Strength Based on Electrical Resistivity Changes

Changes in moisture content, porosity, cation exchange capacity, solutes in the pore water, and temperature influence the resistivity of the soil. In the following analysis, we assume that only moisture content and pore water resistivity are important because these are the only two parameters that are likely to change during the infiltration test. If the only change caused by the infiltration is a saturation increase, then the bulk electrical resistivity will typically decrease. If the only change is an increase in the pore-water resistivity, then the bulk resistivity will increase.

Waxman and Thomas (1974a,b) describe a model for electrical conduction in partially saturated shaly sands typical of oil reservoirs, which accounts for conduction through the bulk pore water as well as conduction through the electrical double layer near the pore surface. Of course, it also models the saturation dependence of the resistivity. We will use this model to account for changes in pore-water resistivities and to estimate changes in soil saturation.

Waxman and Thomas begin with a parallel circuit model for conductance

$$\mathbf{C = \frac{1}{F^*}(C_W + BQ_V)} \tag{2}$$

where

C	=	the conductivity or 1/R where R is the resistivity
F^*	=	the formation factor or f^{-m} where f is the porosity and m the porosity exponent
C_W	=	the pore water conductivity
B	=	the equivalent conductance of counterions on the double layer
Q_V	=	the effective concentration of exchange cations.

The first term represents conductance through the bulk pore water while the second term is the conductance along the double layer. This expression can be modified for partially saturated media by realizing that the first term is just Archie's equation, and $Q/S = Q_V$ where S is the fractional saturation. In terms of resistivity, Equation 2 can be re-written as:

$$\mathbf{R = \frac{R_W \phi^{-m} S^{1-n}}{S + R_W BQ}} \tag{3}$$

where the exponent n is approximately 2, the saturation index in Archie's modified equation, and R_W is the water resistivity. Waxman and Thomas reported results that suggest that m is approximately equal to n. When $R_W BQ >> S$, the electrical double layer is the primary conduction pathway. When $R_W BQ << S$, the primary conduction pathway is through the open pore space. For the analysis that follows, we will assume that the primary conduction pathway is through the open pore space. We make this assumption because the sands at the site have relatively low cation exchange capacity.

We can use Equation 3 in ratio form to calculate resistivity changes in the form of resistivity ratios. When the primary conduction pathway is the through the water in the open pore space, the resistivity ratio is:

$$\frac{R_a}{R_b} = \frac{R_{w,a}}{R_{w,b}} \left(\frac{S_b}{S_a}\right)^2 \tag{4}$$

where R_b and R_a is the resistivities before and after infiltration started and $R_{w,b}$ and $R_{w,a}$ are the water resistivities before and after infiltration. S_b and S_a are the saturations before and after infiltration started. This equation indicates that saturation changes have a strong influence on the observed bulk-resistivity changes. Bulk-resistivity changes are also affected by changes in pore water resistivity, but they are less important than the saturation changes.

Using Equation 4, we can calculate an image showing the changes in saturation shown by the spill. This calculation requires that the quantity $\frac{R_{w,a}}{R_{w,b}}$ be defined. At the time of writing, there were no samples of the pre-spill or post-spill pore waters to determine the value $\frac{R_{w,a}}{R_{w,b}}$. To avoid this dilemma, we have chosen to adjust the value for $\frac{R_{w,a}}{R_{w,b}}$ such that the $\frac{S_a}{S_b}$ obtained from the resistivity tomograph is consistent with the volumetric water content changes detected by the neutron surveys.

We had to interpolate the neutron data in 3-D space as described previously to compare the neuron data with the ERT images. Using the interpolated volumetric water content based on neutron data, we can calculate a volumetric water-content difference. This difference is then used in a mass balance analysis that determines the increase in the pore-water volume resulting from the spill. The change in pore-water volume can then be compared to the volume of the spill water to infer how much water remains in the monitored region and how much water has escaped. The mass-balance analysis suggests that after the first two spills, the pore-water volume increased by approximately 8500 L. This analysis is based on neutron surveys collected before the spill on 5/5/00 and another collected right after the end of the second spill (6/9/00). The actual released volume after the first two spills was 8000 L. The discrepancy indicates that there is some error in the interpolated values. More importantly at present, the neutron data suggest that most, if not all, of the water released remains in the pore space within the region of interest.

To calculate $\frac{S_a}{S_b}$ based on resistivity data, we will assume that all of the 8000 L released after the first two spills remain within the survey volume. We will then do a mass-balance calculation that uses the resistivity and neutron results as follows:

$$V_{a,r} = \frac{S_a}{S_b} * V_{b,n} \tag{5}$$

and

$$\Delta V = V_{a,r} - V_{b,n} \tag{6}$$

where ΔV is the change in volumetric water content, $V_{a,r}$ is the volumetric water content at the end of the second spill based on the resistivity changes, and $V_{b,n}$ is the pre-spill, neutron volumetric water content. Then we adjusted $\frac{R_{w,a}}{R_{w,b}}$ in Equation 4 such that $\Delta V = 8000$ L. Figure 5.10 shows the change in moisture content from this analysis of the ERT and neutron data for the combined effects of Spills 1 and 2. For comparison, it also shows the moisture plume for the combined spills as seen only in the neutron data.

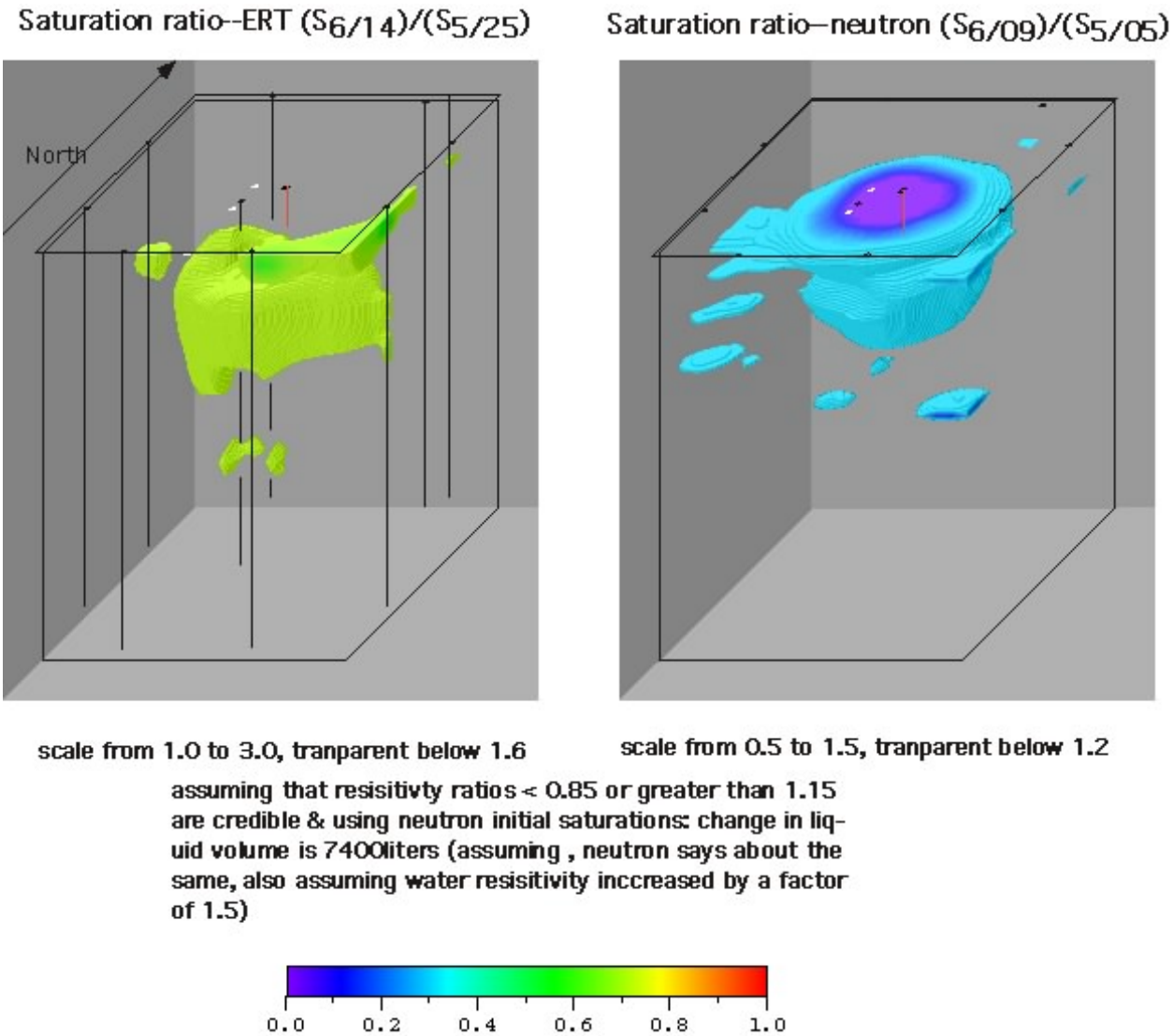

Figure 5.10. Comparison of the ERT and Neutron Data Showing the Plume from Spills 1 and 2. At left is the ERT image of the plume generated from changes in electrical properties interpreted using a petrophysical model relating them to moisture-content changes. On the right is the corresponding plume generated from an interpolation of the neutron data.

For the first two spills, this approach also indicates that $\frac{R_{w,a}}{R_{w,b}}$ should be about 2 (on average) in order for $\Delta V = 8000$ L. This result suggests that the average resistivity of the water in the pore space doubled during the course of the infiltration. One possible interpretation is that the pre-spill pore water was enriched in ions (higher ionic strength) relative to the spill water. As the spill progressed, these excess ions were flushed out of the system or diluted by the relative fresher spill water.

We now turn our attention to the changes in ionic strength caused by the spill of the KBr solution. Four thousand liters of the KBr solution were released about 1 week after 8000 L of fresh water had been released. This means that the KBr solution was released into very wet soil. The electrical conductivity of the KBr solution was approximately 16 times higher than that of the fresh water used for the previous two spills (fresh-water conductivity was 140 microSiemens/m while the KBr solution conductivity was 2200 microSiemens/m). In terms of Equation 4, the infiltration of KBr waters into very wet soil means that $\frac{S_a}{S_b}$ is approximately 1 and that $\frac{R_{w,a}}{R_{w,b}}$ may range between 1 and $^1/_{16}$. Thus, the dominant reason for resistivity to change during the KBr release was the increase in ionic strength of the pore water affected by the release.

We will use the bulk resistivity changes caused by the KBr spill to infer the changes in pore water resistivity, $\frac{R_{w,a}}{R_{w,b}}$. In this analysis, we will use Equation 4 re-arranged and the neutron interpolations (to determine $\frac{S_a}{S_b}$). We will then use the $\frac{R_{w,a}}{R_{w,b}}$ tomograph to calculate the amount of mixing of the KBr solution penetrating the pore space and the pre-KBr spill pore water. The following equation is used:

$$R_{w,a} = R_{KBr}F + R_f(1-F) \tag{7}$$

where R_{KBr} is the resistivity of the KBr solution (4.5 ohm-m), R_f is the resistivity of the pre-KBr spill pore water (assumed to be the same as the resistivity of the fresh water used during the first two spills, 71.5 ohm-m), and F is the fraction of the KBr tracer at the end of the release. Note that when F = 1 ($\frac{R_{w,a}}{R_{w,b}}$ = 4.5/71.5 = 0.061), all of the liquid in the pore volume is KBr tracer at full strength and when F approaches 0, there is very little KBr in the pore space.

Figure 5.11 shows the results of this analysis. Note that the left image shows that the mixing criterion where all of the pore fluid is KBr is the result where F = 1. None of the voxels meet that mixing criterion. For the F = 0.8 case (second image from the left), a few of the voxels just below the injection point met the mixing criterion of 80% when the pore fluid is KBr. As F continues to decrease in the remaining images, more and more voxels are shown in the images. For the image showing F values at or above 0.4, note that most of the voxels are just below and to the South and East of the injection point; also, most of the voxels are located above the 12-m depth. The results in Figure 5.11 suggest that the original pore fluid was largely replaced by the tracer fluid in a volume directly below the injection point (e.g., images F

> 0.6). This region of fluid replacement is relatively compact in depth and volume—notice that at about 4 m from the release point, F is already at 0.4.

The reliability of the results in Figure 5.11 is limited by differences in the times in which the neutron and resistivity data were collected. The ERT data were collected the day before and the day after the KBR solution was released. The neutron data were collected 5 days before the start of the KBr spill (the day after the second fresh water release ended) and the day after. Thus, it is probable that the $\frac{S_a}{S_b}$ determined from neutron data represents a somewhat different saturation condition than that sampled by the resistivity surveys.

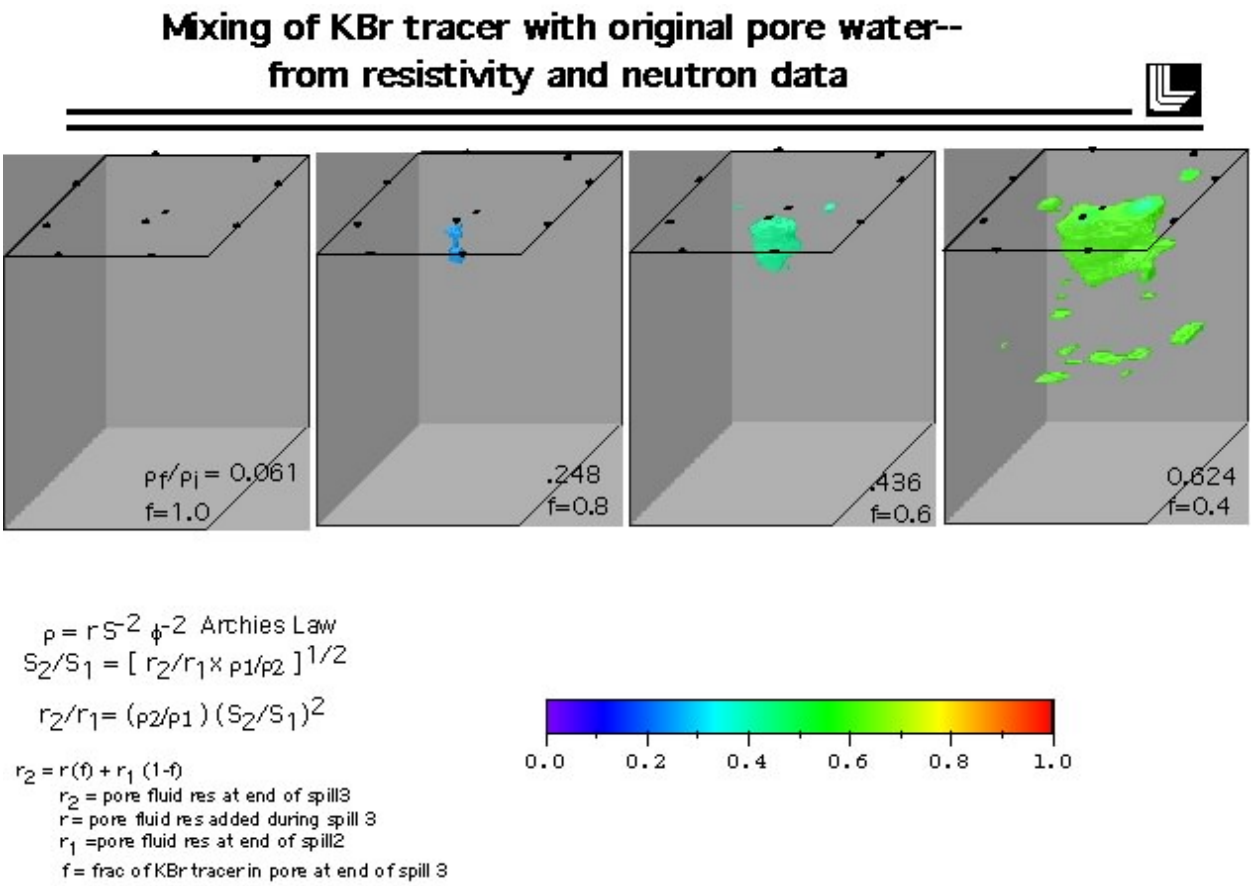

Figure 5.11. ERT Images of the Effects of Mixing of Tracer Water and Native Pore Water. At left is the image showing no voxels with 100% KBr tracer in the pores. Very close to the release point there are a few voxels with 80% of the pore volume (f=0.8) occupied by the tracer water. A larger volume of soil is identified for f=0.6 where 60% of the pore volume is filled with tracer.

5.7 Possible Tank Farm Deployment Scenarios-—Using

Existing Steel Casings as Electrodes

Monitoring for leaks and plume movement under tank farms is a problem of interest to DOE. If one could easily and cheaply drill boreholes around existing tanks, monitoring for leaks and plume movement using ERT would be relatively straightforward and has been demonstrated as described by Ramirez et al. (1996) and Iwatate et al. (1996). A key problem in implementing this approach is the cost (and risk) of drilling boreholes within a tank farm. Here we consider other possible deployment scenarios that do not require drilling within a tank farm, and test their effectiveness using data from the infiltration tests.

The simplest and cheapest tank farm deployment scenario would involve the installation of electrodes only at the ground surface. In many situations, this arrangement has been shown to be useful. However, in a tank farm, surface electrodes are unlikely to be useful for the following reasons. The metal tanks are 75 ft in diameter, 50 ft. tall, and are very good electrical conductors. If electrodes are placed at the surface, currents will be channeled into the tanks themselves; little, if any, current will reach below the tanks. This will greatly reduce sensitivity under the tanks. The distance between adjacent tanks (usually about 25 ft) is small compared to a tank's diameter. Therefore, moving electrodes away from a tank to get some of the current to sample the soil below the tank will only move those electrodes closer to adjacent tanks. As a result, it is very difficult to sample the soil below the tanks using surface electrodes.

Successful ERT below a tank farm requires the ability to produce significant current below the tanks. One option that does not require additional drilling is to use the steel casings of the so called "dry wells" as (long) electrodes. Around each tank, there are usually a few to several steel-cased boreholes that extend below the tank bottom. By connecting a wire to each of them at the ground surface, it is possible to direct a small amount of current beneath the tanks. This approach would only allow low resolution (there are few of them) horizontally and little or no resolution vertically (currents are predominately horizontal). We have used the steel casings at the test sites as surrogates for the dry wells.

On May 26th, as a baseline, and after releases 1, 2, 3, and 5, we took data for the purpose of imaging the released tracer using only the steel casings at the site as "long" electrodes. Data were taken using wells A1,A3, A5, B2, B4, B6, C1, C3, C5, D2, D4, D6, E1, E3, E5, F2, F4, F6, G1, G3, G5, H2, H4, H6. We successfully reconstructed values of transfer resistance R_D measured after each release, using Equation (1) in exactly the same way as described above. Each casing was modeled in the 3-D finite difference mesh as a 1-D anomaly 10^4 times more conducting than the surrounding voxels.

The results for releases 1, 1 and 2 combined, and 3 are shown in Figure 5.12 through Figure 5.14. Figure 5.12, comparing data from June 1st and a May 26 baseline, shows the effects of the first release. Figure 5.13 compares June 14th (just prior to Release 3) and June 1st data and therefore includes the combined effects of the first and second release. Figure 5.14 compares June 14th as baseline and June 16th (just after the 3rd release) and therefore represents the effects of only the 3rd release. Notice that the anomaly images are located at the top of the image block. The vertical extent of each anomaly is artificial—it does not represent the actual depth extent of the plume—but rather is controlled by the value set in the finite element mesh for the conductivity of the steel casings. Infinitely conducting casings would produce a uniformly conducting anomaly in the vertical direction.

Notice that each analysis yields a conducting anomaly, correctly representing the horizontal location of the tracer water plume, directly below the release point. Because of the crude sampling of the image

volume using electrodes that are as long as the image block is deep, only a crude image of the plume should be expected. We believe these images demonstrate that steel casings can be used to produce rough maps of the horizontal location of plumes.

Another approach that we have considered is a logical extension of the "long" electrode approach described above. In this case, we assume that boreholes can be drilled some distance away from the tank farm perimeter, and vertical electrode arrays are installed in them. The vertical electrode arrays are then used in combination with the steel-cased dry wells to sample the soil around and underneath the tank farms. This approach offers the possibility of resolving plumes vertically as well as horizontally.

To demonstrate this approach, we have combined the "long" electrode data with data collected using the vertical electrode arrays. Measurements in the combined data set that used electrodes in the center vertical array were removed to simulate the case where no electrode arrays are installed within a tank farm. This data set is collected as though electrode arrays could be installed outside the farm's perimeter, and the "dry wells" could be used as electrodes inside the farm. We will discuss the results of this approach next.

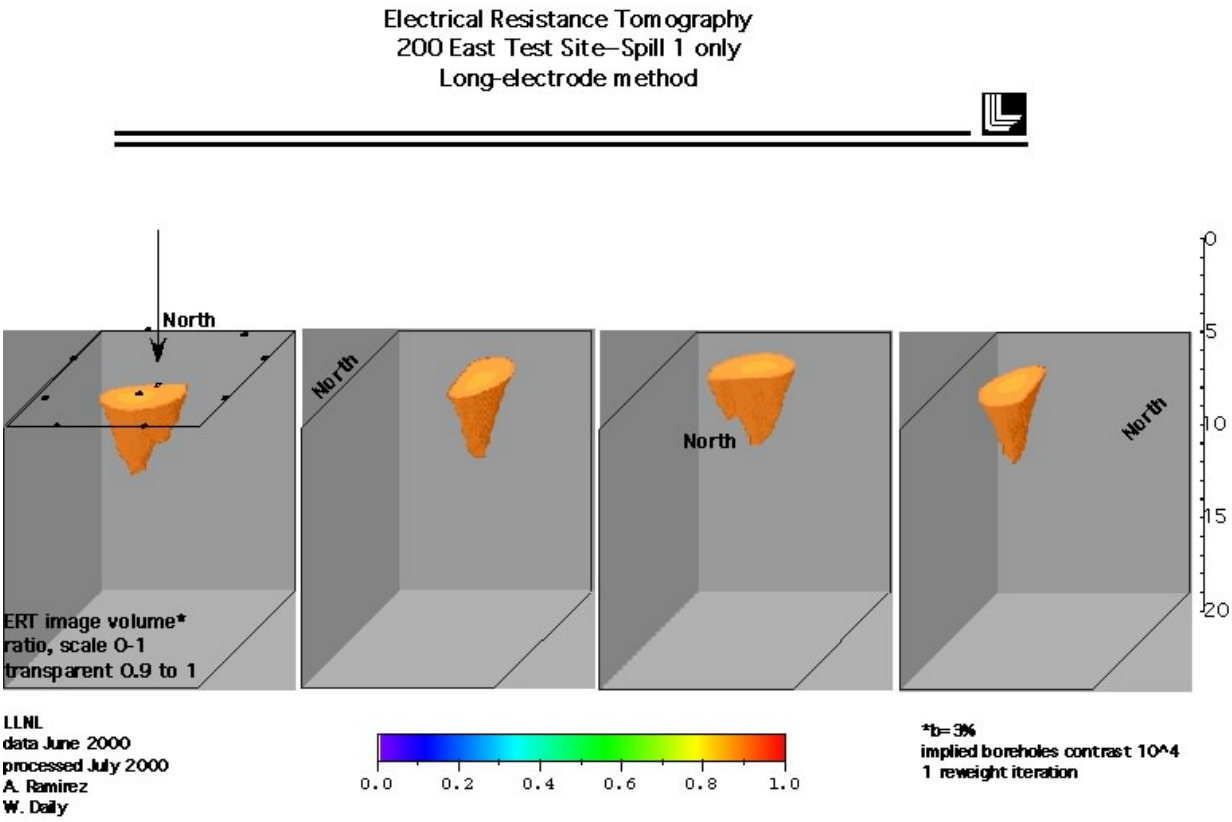

Figure 5.12. Four Views of the Electrical Anomaly from Spill 1 Reconstructed Using only the Steel Casings as Electrodes

"Long" electrode data (24 casings) and vertical array data (using only the eight arrays on the perimeter of the site—no center electrode array) were collected before the first water release and 5 days after the second release. These data were combined as described above and processed in the same manner, and the previously described reconstructions were performed. The results are shown in the image on the right in Figure 5.15. The image on the left of the figure is the equivalent result obtained when all the point electrode data are used, but no long electrode data are used. Note that the image on the right shows an anomaly primarily at the southeast quadrant of the block. The depth of the anomaly extends about 3 m below the top of the block. A comparison of the two images in Figure 5.15 suggests that the image with all the vertical-array data shows a more compact and detailed anomaly than the right image. This probably means that the image with all vertical-array data offers the highest resolution and most sensitivity to the plume. This is to be expected because there is about four times as much data for this reconstruction as for the one using limited vertical arrays with the casings. However, the image combining the vertical array and long electrode data does offer some resolution both laterally and vertically. This suggests that the use of vertical electrode arrays around the perimeter of a tank farm together with the use of the "dry wells" may provide reasonable images of plumes beneath a tank farm.

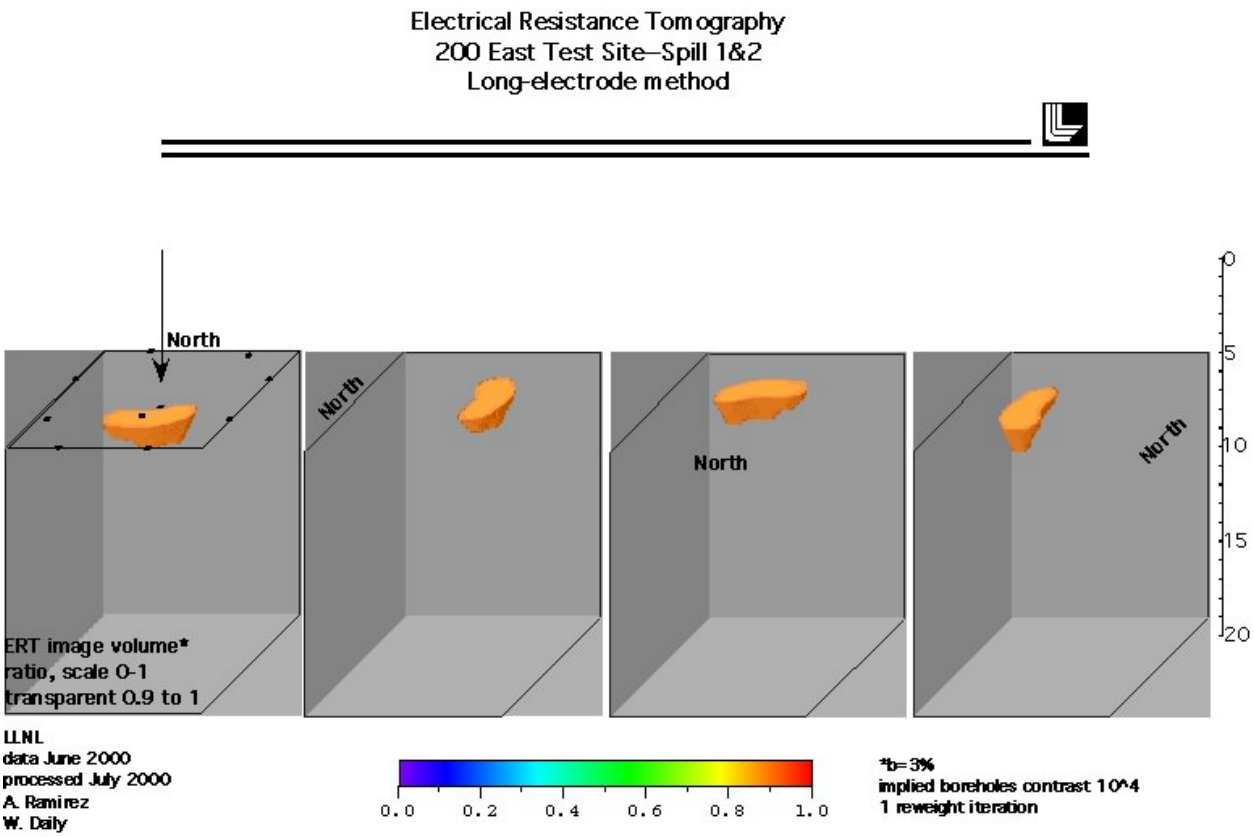

Figure 5.13. Four Views of the Electrical Anomaly from Spills 1 and 2 Reconstructed Using only the Steel Casings as Electrodes

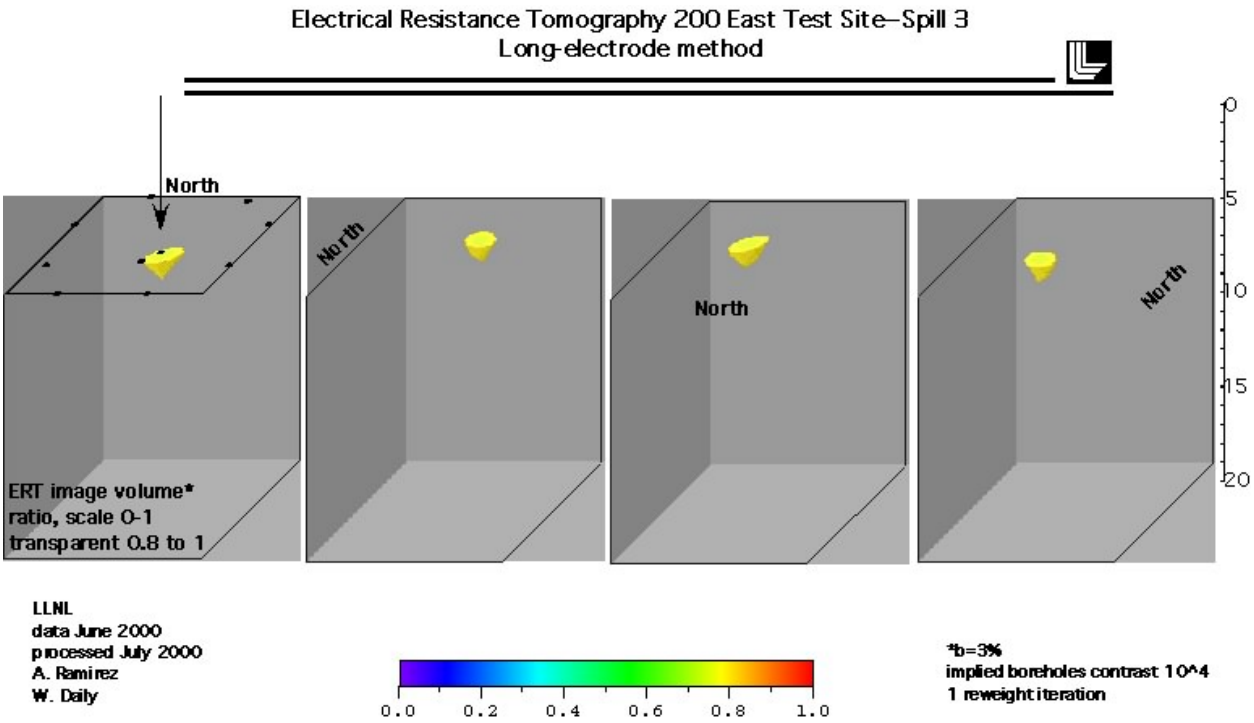

Figure 5.14. Four Views of the Electrical Anomaly from Spill 3 Reconstructed Using only the Steel Casings as Electrodes

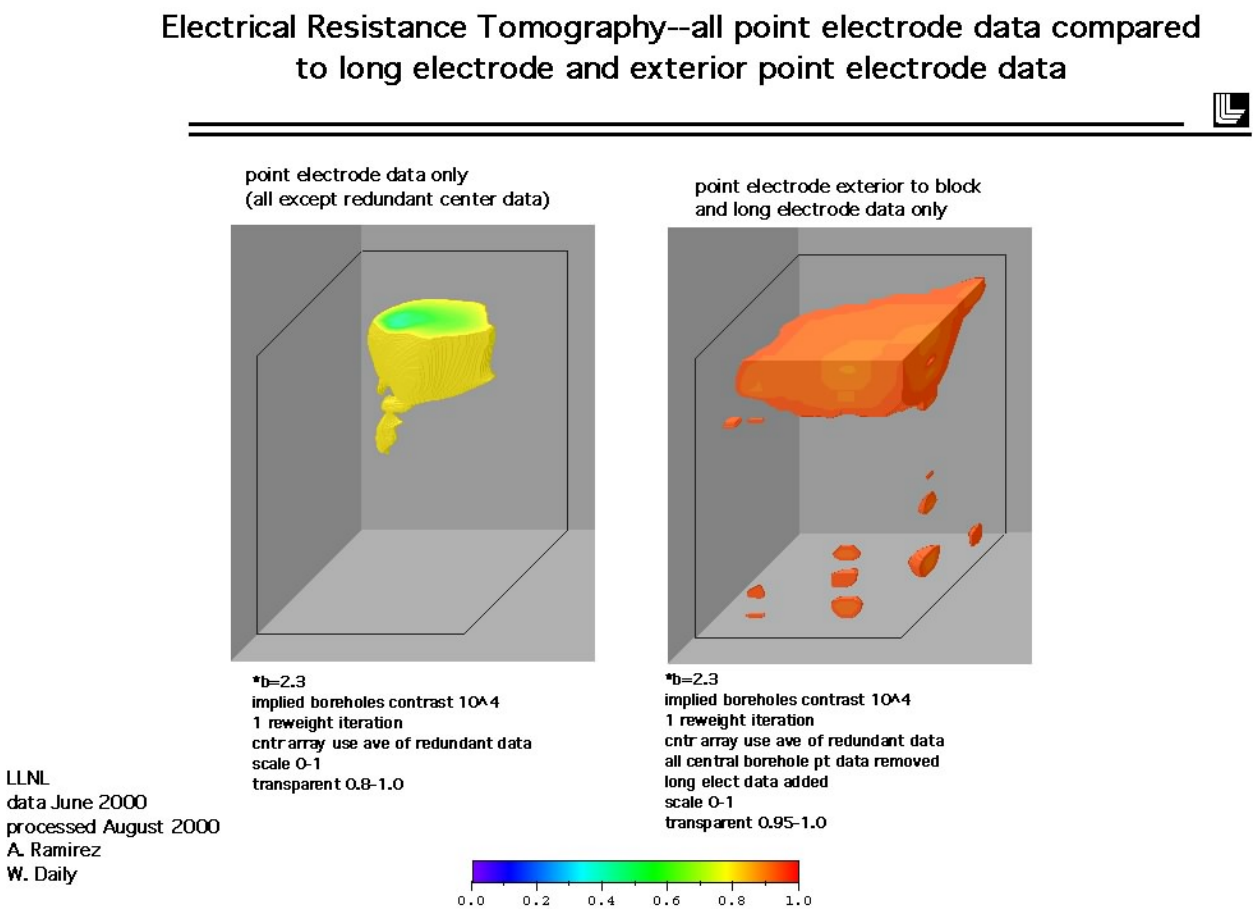

Figure 5.15. ERT of Spill 3 Using Data as they Might be Available at a Tank Farm. For the image on the right, all the long electrodes were used as surrogates for dry wells in a tank farm. In addition, all point electrodes on the edge of the image block were used (the center array was not used) as surrogates for electrodes in wells drilled around the periphery of a tank farm. The image on the left is from all point electrode data (including center well)-—see Figure 5.7.

6.0 Summary and Conclusions

From this work, we can draw conclusions about both the attributes of ERT and about the physical response of the subsurface during the experiment. We conclude the following about the attributes of ERT from this work:

ERT works at the site it when the effects of the many steel casings are properly modeled.

- Steel casings create serious electrical short circuits that affect the sensitivity of all EM methods, especially in the vertical direction.
- Differential ERT yields acceptable results with proper modeling of the steel casings.
- Absolute ERT is not possible at this site with current modeling tools.
- The steel casings can be used as long electrodes to produce images of coarse resolution.

Differential ERT compares reasonably well with neutron differences to show the tracer plumes.

- -The location and general size of the ERT and neutron plumes agree.
- -A mass-balance calculation from the neutron data and the ERT data is realistic.

ERT is consistent with tank farm deployment.

- The dry wells can be used as long electrodes for ERT
- The dry wells can be supplemented with other electrodes outside the tank farm to do ERT under the tanks
- It has a demonstrated sensitivity to plumes in this environment
- It would require no new drilling in a tank farm.

We concluded the following about the hydrology of the test:

- The tracer water transport was largely as expected; a bulbous anomaly formed below the release point, and this anomaly tended to move to the southeast. Some of the tracer may have been lost to the image block to the Southeast but most was retained inside the image block. Most of the tracer volume remained above the 11.5-m depth. The initial pore water had a higher electrical conductivity (ionic concentration) than the tracer water in Releases 1 and 2. During the KBr release, the original pore fluid was largely replaced by the tracer fluid directly below the injection point, but this effect decays rapidly away from the injection point.

7.0 Recommendations

Longer term tests would help identify natural conditions at the site. For example, what is the long-term fate of the tracer from this year's experiment? It would be useful to watch the movement of the plume for 6 to 12 months to see long-term effects. Long-term monitoring would also help assess the effects of rainwater infiltration on the site's hydrology.

All of the electromagnetic methods would benefit from building a new test site having few or no steel casings. At such a site, we could obtain 3-D images of baseline electrical properties and 2-D slices as a function of time during transient conditions. The absence of the steel will increase the sensitivity and resolution of the EM methods, particularly the ability to resolve the vertical distribution and shape of the anomalies.

It would be wise to include realistic tank farm conditions into tests. Laying out steel mesh along the ground's surface to simulate the bottom of a metallic tank could simply do this. The tank-leak test facility at the 200 East area could also be considered for use.

It is possible to invert the phase as well as the magnitude of the electrical signal and so obtain impedance tomographs. This additional parameter (phase) relates to several things, including subsurface clay content, saturation, and pore water ionic content. This approach could be used during future tests to better understand vadose zone transport.

Carle and Ramirez (1999) have recently shown how remote, broad coverage provided by geophysics and localized information like core logs can be statistically combined to give a reliable and coherent picture of a site. This approach results in images of site properties that honor both the geophysical data (in the form of ERT, radar, or EM tomographs) as well as other data, such as core logs and well logs. This is a powerful analytical tool that uses all available data and results in very realistic images of the subsurface that are consistent with the data available.

8.0 References

Daily, W. D., W. Lin and T. Buscheck, 1987, Hydrological Properties of Topopah Spring Tuff: Laboratory Measurements, *J. Geophys. Res.,* **92***,* 7854-7864.

Daily, W. D., A. L. Ramirez, and R. Johnson, 1998, Electrical Impedance Tomography of a Perchloroethylene Release, *J. Env and Eng. Geophysics.,* **2,(3)***,* 189-201

Carle, S., and A. Ramirez, 1999, Integrated Subsurface Characterization Using Facies Models, Geostatistics, and Electrical Resistance Tomography, Lawrence Livermore National Laboratory, UCRL-JC-136739, Livermore CA

Henderson, R.P., and Webster, J.G., 1978, An impedance camera for spatially specific measurements of thorax, *IEEE Trans. Biomed Eng*., BME 25, 250-254.

Iwatate, D., S. Narbutovskih, M. Sweeney, W. Daily, A. Ramirez, R. Morey, and L. Christensen. 1996. *Feasibility of CPT deployed vertical electrode array in single shell tank farms,* WHC-SD-EN-TA-004, Rev 0, Westinghouse Hanford Co., Richland, Washington.

LaBrecque, D. J., A. Ramirez, W. Daily, A. Binley, and S. Schima. 1996a. "ERT Monitoring of Enviromental Remediation Processes," *Meas. Sci. Technol.*, vol. 7, .pp. 375-383.

LaBrecque, D. J., Miletto, M., Daily, W. D., Ramirez, A. L., and Owen, E., 1996b, The effects of noise on Occam's inversion of resistivity tomography data, *Geophysics*, **61**, 538-548.

LaBrecque, D., Morelli, G., Daily, W., Ramirez, A., and Lundegard, P., 1999, Occam's inversion of 3D electrical resistivity tomography, in Oristaglio M., and B. Spies, Eds., Three Dimensional Electromagnetics,: Soc. Expl.Geophys.

Lytle, R. J. and K. A. Dines, 1978, An impedance camera: A system for determining the spatial variation of electrical conductivity, Lawrence Livermore National Laboratory UCRL-52413.

Ramirez, A., W. Daily, D. LaBrecque, E. Owen and D. Chesnut, 1993, Monitoring and underground steam injection process using electrical resistance tomography, *Water Resources Research,* **29(1)**, 73-87.

Ramirez, A., W. Daily, A. Binley, D. LaBrecque, and D. Roelant. 1996. "Detection of leaks in underground storage tanks using electrical resistance methods," *J. Environ. Eng. Geoph.,* Vol. 1, no. 3, 189-203.

Waxman, M.H. and E. C. Thomas, 1974a, Electrical Conductivities in Shale Sands - I. The Relation Between Hydrocarbon Saturation and Resistivity Index; The Relationship between Hydrocarbon Saturation and Resistivity Index, *Journal of Petroleum Technology* (Feb.) 213-218; Transactions AIME, 257.

Waxman, M.H. and E.C. Thomas, 1974b, Electrical Conductivities in Shaly Sands - II. The Relation Between Hydrocarbon Saturation and Resistivity Index; II. The Temperature Coefficient of Electrical

Conductivity, *Journal of Petroleum Technology* (Feb.) 218-225; Transactions AIME, 257.